




# Avalanche structural rearrangements in cold dusty plasma liquids through cascaded coherent excitations of heterogeneous multiscale thermal acoustic waves

Hao-Wei Hu , Yi-Cheng Zhao , and Lin I 

Department of Physics and Center for Complex Systems, National Central University, Zhongli 32001, Taiwan, Republic of China



(Received 14 January 2022; accepted 16 April 2022; published 13 May 2022)

Microscopically, the cold liquid around freezing consists of crystalline ordered domains supporting thermally excited acoustic wave turbulence. Whether and how the above uncertain multiscale waves can lead to uncertain avalanche microstructure rearrangements in the form of multiscale clusters, and identifying their precursors, are elusive fundamental issues. Here, using a cold quasi-two-dimensional dusty plasma liquid as a platform, we experimentally address the above issues, especially the extreme avalanche activities, by correlating avalanche dynamics with the spatiotemporal evolutions of local structural order, defects, and the local amplitudes and phases of various wave modes. It is found that the preceding larger skeleton of poor structural order around more and widely spread defects can facilitate the later sequential multiscale wave excitations from slow to fast modes and their cascaded intermittent phase synchronizations for bond-breaking/reconnection and structural rearrangements. It is the key for the onset, spreading with defect propagation, and termination of the large avalanche cluster.

DOI: [10.1103/PhysRevResearch.4.023116](https://doi.org/10.1103/PhysRevResearch.4.023116)

## I. INTRODUCTION

Avalanche activities excited by slow or stochastic drives widely exist in various nonlinearly coupled complex systems. Solid or glass cracking [1–4], seismic activities [5–7], epidemic spreading [8], power blackouts [9,10], and excitations in chemical reaction diffusion systems [11] are good examples. Through the interplay of perturbation and mutual coupling, avalanche activities can uncertainly occur, spread, and terminate, in the form of clusters with a power-law size distribution in the spatiotemporal space, over a certain range of perturbation strength, before the outbreak percolating transition [8,12–14]. Unraveling the generic behavior of the generation and spatiotemporal spreading of avalanche activities—especially the extreme activities with cluster sizes at the power-law distribution tail [8,14]—and identifying their precursors are open important issues.

Microscopically, the cold, supercooled, or glass forming liquids around freezing are strongly coupled complex systems exhibiting structural and dynamical heterogeneities. The competition between the strong mutual interaction under solid-like dense packing and weak thermal agitations leads to the formation of crystalline ordered domains (CODs) with various sizes and orientations, and defect clusters around their interfaces [15–22]. Dynamically, particles alternatively exhibit small-amplitude rattling in cages formed by their neighboring particles and avalanche like cooperative hopping after accumulating sufficient constructive perturbation. The latter in turn causes avalanche-like structural rearrangements (SRs)

through changing nearest neighbors [17–19,22–27]. Recent studies further demonstrated that, in the two-dimensional (2D) cold liquid around freezing, a COD can be cracked and healed through the thermally excited corotations of various sized CODs [27]. It leads to SRs propagating with dislocation defects along the strongly sheared strips between the interfaces of adjacent corotating CODs. Those SRs through bond breaking/reconnection activities can be viewed as avalanche activities [27,28].

Past studies on SRs for liquids around freezing mainly focused on the casual correlation of *local* structural and dynamical variables and the following *single* SR event for identifying predictors for SRs [29]. For example, studies on colloidal glass forming liquid found that local SR tends to occur at the local soft spot, identified through various structural parameters, such as bond orientational orders [18], machine-learning-based order [30,31], coarse grained local structural orders [32,33]; or identified using various *local* dynamical variables such as the short time average intensities of the *local* fast cage rattling [26,34,35] and low-frequency oscillations [36–39]. The amplitudes of the slow acoustic modes obtained from normal mode analysis were found to be good predictors for SRs [36–39]. However, the physical origins of the uncertain emergence, spread, and termination of avalanche SRs are elusive.

In the cold liquid around freezing, CODs and surrounding defects can facilitate and frustrate thermally excited longitudinal and transverse acoustic waves (phonons), respectively, because CODs can temporarily sustain shears [40]. Previous studies also showed that wave excitations, especially the slow modes, are correlated with the heterogeneous microstructure [39,41,42]. It was also demonstrated that those acoustic waves exhibit heterogeneous self-similar coherent excitations at different wave scales, in the form of clusters in the spatiotemporal space [42].

Published by the American Physical Society under the terms of the [Creative Commons Attribution 4.0 International](https://creativecommons.org/licenses/by/4.0/) license. Further distribution of this work must maintain attribution to the author(s) and the published article's title, journal citation, and DOI.

Namely, the heterogeneous microstructure (CODs with various orientations and surrounding defects) affects particle mutual interaction, and consequently the heterogeneous excitation, propagation, scattering, and coupling of thermally excited multiscale acoustic waves. The superposition of multiscale waves in turn determines individual particle motions and positions, and consequently the evolutions of CODs, defects excitation and propagation, and avalanche SR excitations. It is thereby intriguing to unravel the following unexplored issues: (a) how the wave modes at different scales are spatiotemporally correlated with the structural and dynamical heterogeneities, and how their interplay initiate the uncertain SRs followed by their spreading associated with defect propagations, and (b) whether precursors for avalanche SR excitations, especially the extreme avalanche SRs, can be identified from excitations of multiscale waves.

Here, using a quasi-2D dusty plasma liquid as a platform, these issues are experimentally addressed. Through MCEEMD (multidimensional complementary ensemble empirical mode decomposition) [43–46], the relative transverse displacements of pairs of adjacent particles are decomposed into acoustic wave modes with different scales [42]. It is found that avalanche SRs appear in the form of clusters in the  $xy$  space exhibiting power-law cluster size distributions. The larger clusters have larger spatial and temporal spans preceded by larger spatial spans of defects before the onsets of avalanche SRs. A clear dynamical picture is constructed to unify how the interplay of (a) the spatiotemporal evolutions of defects, local and coarse structural order, and (b) cascaded multiscale wave excitations from the slow to the fast modes and their intermittent synchronization lead to the excitation, spreading, and termination of avalanche SRs, especially the extreme SRs in the spatiotemporal space.

MCEEMD is an empirically based method. Unlike conventional Fourier type and instantaneous normal modes analyses [36–39,41,42,47,48], MCEEMD can spontaneously decompose the multiscale dynamical variable into modes at different scales and extract the local instantaneous phases and amplitudes of various modes for reconstructing their spatiotemporal waveform evolutions. It has been successfully used in previous macro- to microscopic wave turbulence studies [42,49–51], especially for identifying extreme events [50,51].

The dusty plasma liquid can be formed by micrometer sized particles suspended in low pressure rf discharge [17,21,22,27,28,42,47,48,52–57]. Particles are negatively charged ( $\sim 10^4 e/\text{particle}$ ) and interact through the screened Coulomb interaction in the plasma. It is a good experimental platform for investigating the generic dynamical behavior of a Yukawa liquid at the microscopic level through direct optical visualization of individual particle motions [17,21,22,27,28,42,47,48,52–59].

## II. EXPERIMENT AND ANALYSIS

The experiment is conducted in a cylindrical symmetric rf (radio frequency) low pressure dusty plasma system (see the sketch of Fig. 1), as described in Refs. [27,42]. The weakly ionized glow discharge ( $n_e \sim 10^9 \text{ cm}^{-3}$ ) is generated in 260 mTorr Ar gas using a 14-MHz rf power system operated at

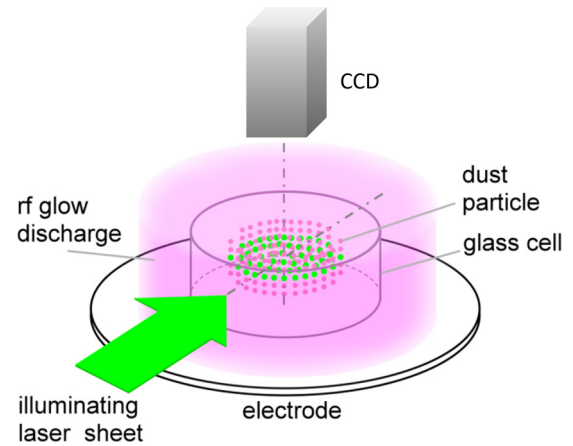


FIG. 1. Sketch of the experimental system, reproduced from Ref. [27].

1.7 W. The dusty plasma liquid formed by polystyrene particles ( $7 \pm 0.4 \mu\text{m}$  in diameter) is confined by the sheath field adjacent to the boundary of a hollow cylindrical trap (4.1 cm inner diameter and 14 mm height) put on the center of the bottom electrode. The estimated Debye length and the charges on particles are in the orders of  $10^{-1} \text{ mm}$  and  $10^4 e/\text{particle}$ , respectively. The wake field effect of the downward ion wind lines up dust particles into vertical chains [59]. Particles along the same vertical chain hop together horizontally, without vertical dust hopping. It makes the system a good quasi-2D system with uniform averaged packing density distribution. In this quasi-2D liquid, particle positions in the horizontal ( $xy$ ) plane, illuminated by a thin horizontal laser sheet, are recorded at 30 Hz sampling rate by a CCD camera on top of the system.

MCEEMD (multidimensional complementary ensemble empirical mode decomposition), an empirical mode decomposition method using the Hilbert-Huang transform [42–46], is used for decomposing thermal acoustic waves into various modes. Through the sifting process,  $D_\alpha(t)$  (the relative transverse displacement) from the local particle pair  $\alpha$  in the  $xy$  plane is successively decomposed in terms of an adaptively obtained, amplitude-frequency modulated oscillatory intrinsic mode function (IMF) with zero mean,  $D_{\alpha,m}(t)$  ( $m = 1, 2, \dots, N$ ), until reaching the mean trend  $r_\alpha(t)$ . Namely,  $D_\alpha(t) = \sum_{m=1}^N D_{\alpha,m}(t) + r_\alpha(t)$  and  $D_{\alpha,m}(t) = a_{\alpha,m}(t) \cos \phi_{\alpha,m}(t)$ . In the sifting process of CEEMD, 200 complementary noise sets are added for avoiding the problems of mode mixing and fake noisy fluctuations on the IMFs. Twenty siftings are applied to obtain each IMF. This complete and nearly orthogonal reconstruction reveals temporal variations of the local amplitude  $a_{\alpha,m}$  and phase  $\phi_{\alpha,m}$  for  $D_{\alpha,m}$ , which can be spatially extended to all particle pairs in the  $xy$  plane. More details of mode decomposition can be found in the Supplemental Material of Ref. [42].

## III. SPATIOTEMPORAL EVOLUTIONS OF STRUCTURAL REARRANGEMENTS, DEFECTS, AND COD ROTATIONS

Figure 2(a) shows two typical snapshots of particle configurations starting at two different times (3 and 21.6 s), and subsequent particle trajectories over a 1.5 s interval. Here,

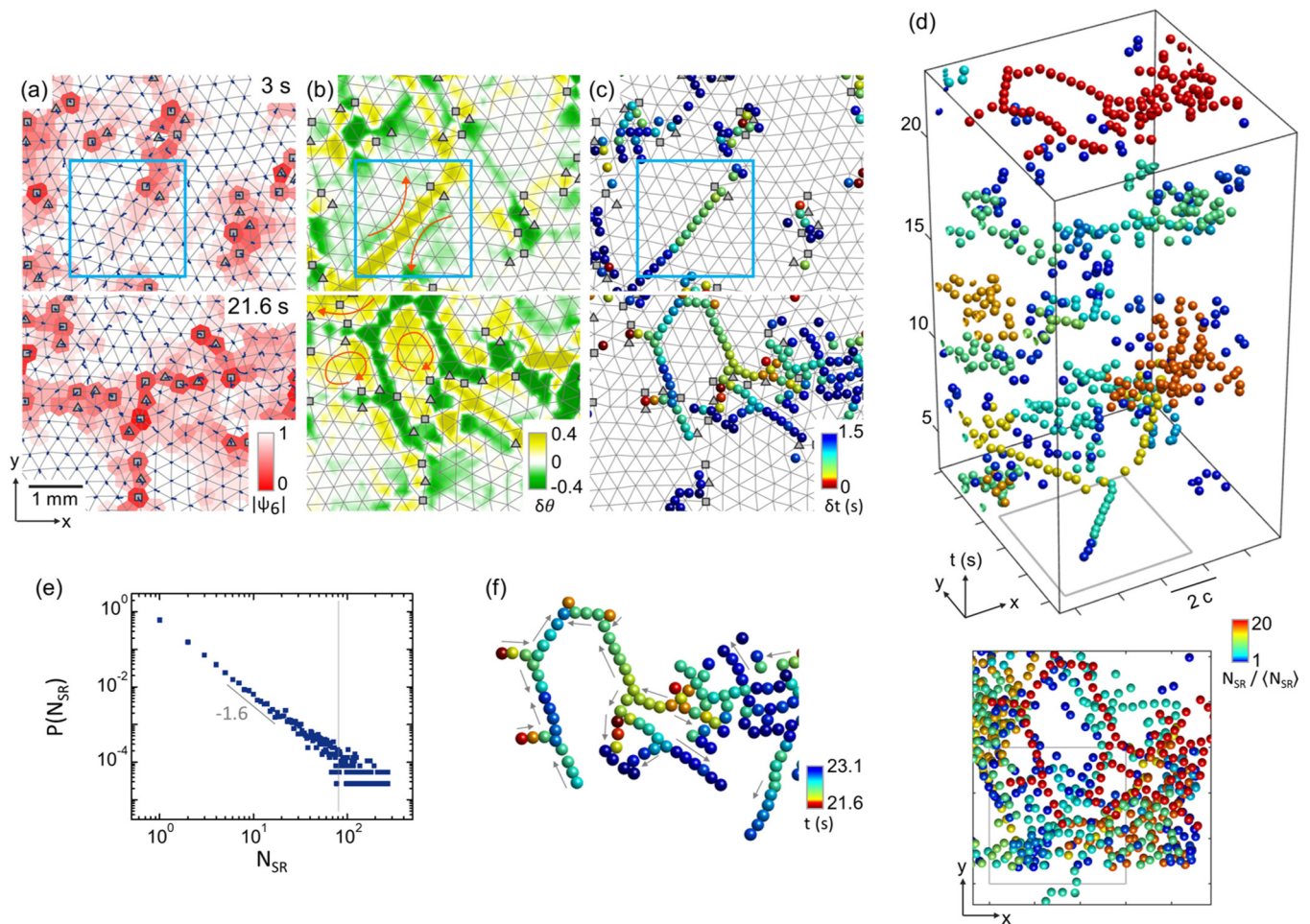


FIG. 2. (a)–(c) Plots of dust particle trajectories color coded by  $|\Psi_6|$ , bond angle variation  $\delta\theta$  over 1.5 s, and SR sites identified by the variations of bond lengths and angles in a 1.5 s time interval, respectively. Particles are located at the vertices of the background grids. Squares and triangles represent sevenfold and fivefold disclination defects, respectively. SR sites are color coded by their occurrence time  $\delta t$  from the starting time of each plot. The arrows in (b) indicate the COD rotation direction. (d) Top panel: SR sites in the form of clusters in the  $xyt$  space, color coded by the cluster size normalized by its mean,  $N_{SR}/\langle N_{SR} \rangle$ .  $c$  is the lattice constant. The squared region is the same as those in (a) to (c). The bottom panel shows the corresponding top view. (e) Probability distribution function of  $N_{SR}$  (the number of SR sites of a cluster in the  $xyt$  space) showing the power-law decay with scaling exponent  $-1.6$ . Clusters with  $N_{SR}$  larger than  $20\langle N_{SR} \rangle$  (the mean cluster size) threshold, as indicated by the gray line, are defined as extreme clusters. (f) Magnified plot of the extreme SR cluster from the bottom panel of (c). The arrows show the examples of SR propagating directions.

particles are located at the vertices of the gray grids, color coded by the magnitude of local bond orientational order  $|\Psi_6|$  ( $= 1$  and  $< 0.4$  for perfect and defect sites, respectively), as defined in Appendix A and Ref. [60]. Squares and triangles represent seven- and fivefold disclination defects, appearing in the form of clusters on the interface of CODs with various sizes and orientations [21,22,27]. Figure 2(b) shows the corresponding configurations color coded by the bond angle variation,  $\delta\theta$ , over the subsequent 1.5 s. Dynamically, particles exhibit stick-slip type cage rattling and cooperative large-amplitude hopping. In Fig. 2(b), the patches coded by lighter green and yellow manifest counterclockwise and clockwise COD rotations (see the arrows indicating the rotation directions), respectively.

The excitation of adjacent corotating CODs generates strong shear strips (color coded by darker green and yellow) on COD interfaces, along which the bonds between two adjacent CODs exhibit large bond length and angle variations. It

can lead to the breaking and reconnection of the lattice lines crossing strong shear strips [27,28]. COD rotation ceases after cracking/reconnection. Namely, these bond cracking-healing sites can be viewed as SR sites, which coincide with the locations of dislocation defects [28]. Figure 2(c) shows the SR sites defined as the sites with bond angle variation greater than 0.25 rad and length variation greater than 15% in a 1 s interval (here 1 s is the typical timescale for the abrupt bond angle and length changes, color coded by the occurrence time  $\delta t$  from the starting time of each exposure, to indicate the propagation of SRs). The same threshold for identifying the SR site is used throughout this work.

The top panel of Fig. 2(d) and Video S1 of the Supplemental Material further show SR clusters in the  $xyt$  space [61]. Here, neighboring SR sites are considered as connected sites if their spatial and temporal separations are shorter than  $1c$  and 0.3 s, respectively, to identify the SR cluster. The SR clusters are color coded by single cluster size  $N_{SR}$  (number of SR sites

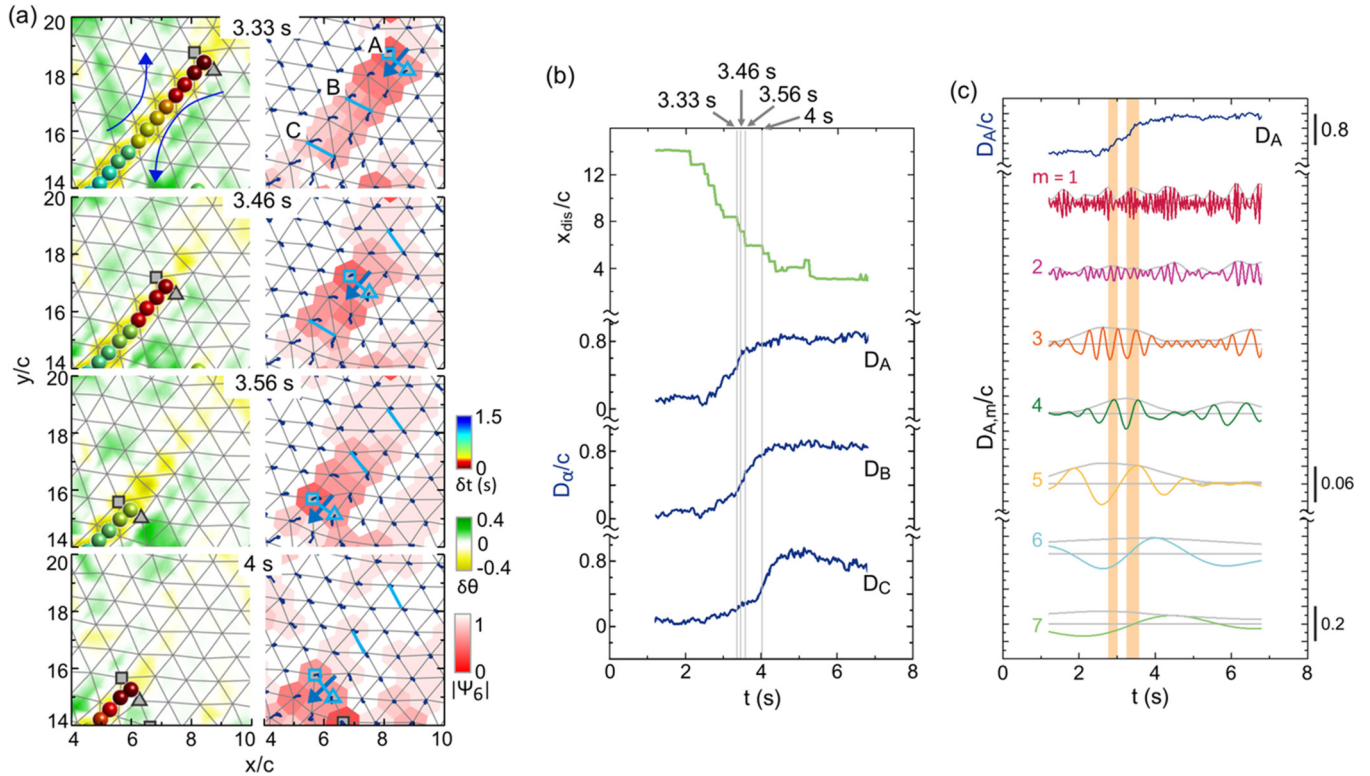


FIG. 3. (a) Left column: sequential snapshots zoomed up from the squared region in the top row of Figs. 2(a) and 2(c), in which the current location of dislocation defects (i.e., 5–7 defect pairs), the SR sites, and bond angle variation over 1.5 s interval are coded using the scheme as in Figs. 2(a) and 2(c). Right column: the corresponding plots with dust trajectories and particle configuration color coded by  $|\Psi_6|$ . The blue arrows normal to the bond connecting the five- and sevenfold disclination pair indicate the defect propagation direction along their Burgers vectors. (b) Temporal evolutions of positions of the dislocation defect in (a),  $x_{\text{dis}}/c$ , and relative transverse displacements  $D_\alpha/c$  of particle pairs A to C. The vertical gray lines indicate the times for the snapshots of (a). (c) Temporal evolutions of  $D_A/c$  (relative transverse displacement of pair A) and its decomposed results  $D_{A,m}$ , for  $m = 1$  to 7, with gray curves indicating the amplitude evolutions. The two orange bands indicate the time intervals in which the fast rising parts of most of  $D_{A,m}$  with large  $a_{Am}$  synchronize, leading to the rapid increases of  $D_A/c$  and the defect slipping.

of a single cluster in the  $xyt$  space), normalized by the mean single cluster size  $\langle N_{SR} \rangle$ . The bottom gray box region is the same region as the square box region of Fig. 2(c). The bottom panel of Fig. 2(d) shows the corresponding top view image. Note that, for better visualization of the large clusters, clusters smaller than two SR sites are not shown.

The corotating large CODs can induce long strong shear strip and dendritic SRs. The cracking of a large COD into several small corotating CODs can induce denser SRs [27,28]. The probability distribution function of  $N_{SR}$  shown in Fig. 2(e) exhibits a power-law distribution with scaling exponent  $-1.6$ . It manifests self-similar dynamical selection rules over different scales for avalanche activities [13,14,28]. We further define the clusters with cluster size greater than  $20\langle N_{SR} \rangle$  [those in the tail of Fig. 2(e) beyond the above threshold indicated by the gray line, i.e., the top 0.5% largest clusters] as extreme avalanche clusters. Figure 2(f) shows the typical extreme avalanche cluster in the  $xy$  space, corresponding to the large cluster in the lower panel of Fig. 2(c), initiating from different sites, labeled by red spheres. Here, SR sites are color coded by their occurrence times. The arrows show the examples of SR propagating directions.

Now let us focus on the details of the dynamical behaviors of bond rotation, and SRs associated with defect propagation,

along the strong shear strip, which is the fundamental building block for the formation of dendritic SR branches of the extreme SR excitations. The example in the left column of Fig. 3(a) shows the sequential snapshots magnified from the squared region in the top row of Figs. 2(a) to 2(c), in which the current location of dislocation defects (i.e., 5–7 defect pairs), the SR sites, and bond angle variation over subsequent 1.5 s interval are coded using the same scheme as in Figs. 2(b) and 2(c). The right column of Fig. 3(a) shows the corresponding plots of the particle configurations color coded by  $|\Psi_6|$ , and the subsequent particle trajectories over 1.5 s. The blue arrows indicate the defect propagating directions along their Burgers vectors normal to the bonds connecting the five- and sevenfold disclination pairs [62].

Figure 3(b) shows the temporal evolutions of  $x_{\text{dis}}$  (the dislocation defect position along the  $x$  axis) and  $D_A$  to  $D_C$  of bonds A to C [the light blue bonds in the right column of Fig. 3(a)]. Here,  $D_\alpha$  is the relative transverse displacement of the particles at the two ends of bond  $\alpha$ , and  $c$  is the mean interparticle distance. The center stage with large change of  $D_\alpha$  (about  $0.7c$  to  $1c$ ), sandwiched between the two stages with small amplitude fluctuations, indicates the stick-slip nature of alternate small amplitude cage rattling and strong bond rotation.

As shown in Fig. 3(a), the counterclockwise corotations of the two adjacent CODs induce the clockwise rotations of bonds in the yellow shear strip. Along the strong shear strip, bond rotation starts from A and propagates successively toward the lower left corner, associated with the gradual drifting of the adjacent COD rotation (see the gradual lower-left drifting of the green region). It indicates that the adjacent CODs do not rotate as rigid bodies. The successive strong rotations of bonds cause successive SRs for the particles at each end of the bond through changing its nearest neighbor number due to rotation. It in turn causes SR propagation associated with the propagation of the dislocation defect along the strong shear strip in a stick-slip way, as shown in the staircase like curve of  $x_{\text{dis}}$  in Fig. 3(b).

For example, as shown in Fig. 3(a), the defect moves from the locations of bond A to bonds B and C from 3.33 s to 3.46 s and 3.56 s, associated with the propagation of bond rotation along the strong shear strip. However, the dislocation defect sticks at bond C until  $t = 4$  s. After 5 s, the viewing zone exhibits a defect-free crystalline ordered structure (not shown).

More examples showing the defect motion along shear strips generating dendritic-like SRs branches can be found in Appendix B.

#### IV. SUPERPOSITION OF LARGE AMPLITUDE MULTISCALE WAVES AND THEIR PHASE SYNCHRONIZATIONS LEADING TO UNCERTAIN AVALANCHE STRUCTURAL REARRANGEMENTS AND THEIR SPREADS

How does the superposition of multiscale transverse acoustic waves lead to the above cooperative motions and the stick-slip bond rotation and SRs? To extract the wave, we decompose the temporal evolution of  $D_\alpha(t)$  of a local bond into amplitude-frequency modulated wave modes with zero mean  $D_{\alpha,m}(t)$  through the sifting process in MCEEMD (see Sec. II). Figure 3(c) shows the examples of the temporal evolutions of  $D_A$  and  $D_{A,m}$  of modes 1 to 7 of bond A, with the gray lines showing the evolutions of the amplitude  $a_{\alpha,m}$ . As illustrated in the orange bands, synchronizations of the strong rising parts of most  $D_{A,m}$  with large  $a_{A,m}$  (modes 7 to 3) are important for the formation of the large change of  $D_A$  in the time interval about 0.3 s. The desynchronization of those slow modes with small  $a_{A,m}$  leads to the small temporal variation of  $D_A$  in regions other than the orange bands. The alternate intermittent synchronization and desynchronization from 2.8 to 3.5 s lead to the alternate slipping and sticking of  $D_A$  variation. The fast modes 2 and 1 mainly contribute to cage rattling (small amplitude wiggling of  $D_A$ ). The intermittent synchronization also leads to the uncertain sticking time for  $x_{\text{dis}}$ .

Note that the large change of  $D_A$  from 2.8 to 3.5 s is preceded by the sequential rises of  $a_m$  from the slow modes to the fast mode 3, and followed by the reverse process in the two cage rattling stages with small  $D_A$  fluctuations [see Fig. 3(c)]. The right column of Fig. 3(a) also indicates that the propagation of the poor structure region (red region) along the strong shear strip precedes the propagations of dislocation defect and SR. After the defect passes by, the structural order

of the trailing region gradually reforms. Namely, the local structural order deterioration and slow mode amplitude rises can be used as local precursors to warn of local SR.

The probability distribution functions of the phases and amplitudes of various modes for different temporal change rates of the local  $D_\alpha$  in Fig. 8 further statistically manifest that the larger  $a_{\alpha,m}$  and the better phase synchronization of various modes are the keys leading to the larger change of  $D_\alpha$  (larger bond rotation rate) for the local SR (see Appendix C).

By extending the above sifting process of  $D_\alpha(t)$  to all particle pairs, the spatiotemporal evolutions of all modes can be obtained. Figure 4 shows SR sites represented by the balls and the surrounding isophase surfaces with  $\phi_m = 3\pi/2$  (i.e., the phase for the fastest increase of  $D_m$ ) for modes 3 to 6 in the  $xyt$  space, color coded by normalized local wave amplitude  $A_m = a_m/\bar{a}_m$ , for the region corresponding to the lower square region of Fig. 2(d) (see Appendix A for the plotting method of the isophase surface). Here  $\bar{a}_m$  is the averaged amplitude over all particle pairs and time of mode  $m$ . The positions of  $\text{SR}_A$  and  $\text{SR}_C$  coincide with the positions of the defects located at A and C in Fig. 3(a), respectively. Note that some isophase surfaces which block the visualization of SRs in Fig. 4 are not shown (see Appendix C for the more complete plots in Fig. 9, and Supplemental Material Video S2 showing the isophase surface from different angles [61]).

The isophase surface of each mode can be considered as the coherent waveform of the large bond angle changes of each mode in the  $xyt$  space. As shown in Fig. 4, the corrugated isophase surface of each mode can intermittently emerge, propagate, scatter, and annihilate in the  $xyt$  space [42]. The amplitudes  $A_m$  of the show modes show earlier rises. As those intermittently emerged coherent waveforms with gradually increasing amplitudes reach the neighborhoods of SR sites, the synchronization of the large increase (or decrease) of local  $D_m$  around  $\Phi_m = 1.5$  (or  $0.5\pi$ ) can lead to the large local change of  $D$ , and consequently induce SRs and their propagation in the  $xyt$  space.

#### V. STRUCTURAL AND DYNAMICAL PRECURSORS FOR LARGE AVALANCHE SR CLUSTERS

What kinds of dynamical and structural information can serve as the precursors of large avalanche SRs? We identify clusters belonging to two different cluster size categories: type I,  $N_{SR} = 17\langle N_{SR} \rangle$ , and type II,  $N_{SR} = 31\langle N_{SR} \rangle$  (extreme avalanche cluster). Here  $N_{SR}$  is the number of SR sites of a single cluster in the  $xyt$  space and  $\langle N_{SR} \rangle$  is the average of  $N_{SR}$  over all clusters. Figure 5(a) shows the waterfall plots of the temporal evolutions of  $\langle A_m \rangle_c$ , the normalized amplitudes of modes 1 to 7, and  $\langle \psi_6 \rangle_c$ , averaged over all the sites in the circled regions at time  $\tau$  for the above two types of SR clusters with different sizes. Here, the center of the circled region is the spatial center of mass of all SR sites in the cluster, and the circle radius is  $5c$ , i.e., 1.25 times of the radius of gyration of the spatial positions of all SR sites in a cluster, averaged over all type II clusters.  $\tau$  is the reset time with  $\tau = 0$  at the time for the initial SR site of each cluster. Each horizontal gray dashed line denotes  $\langle A_m \rangle = 1$  (the mean amplitude over all sites in the  $xyt$  space) for each mode.

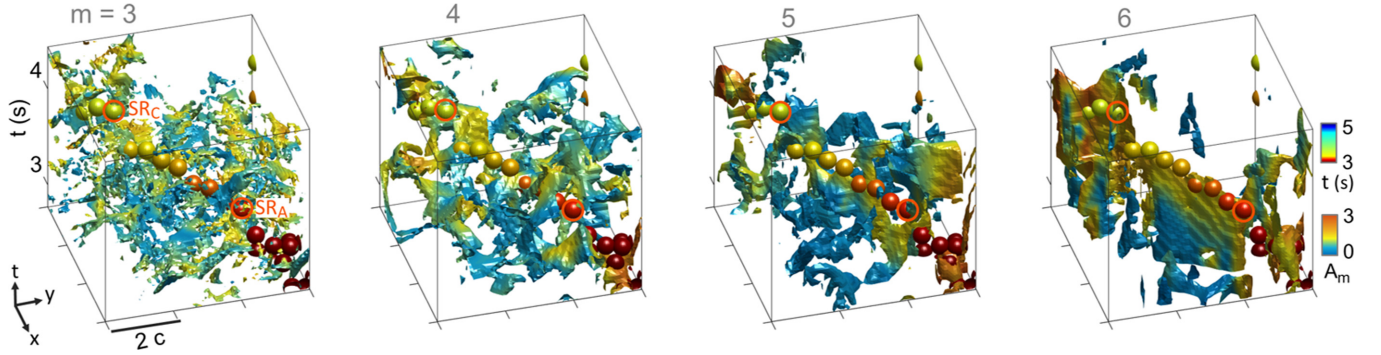


FIG. 4. SR sites represented by the balls color coded by the occurrence time  $t$ , and the surrounding isophase surfaces with  $\phi_m = 3\pi/2$  for modes 3 to 6 in the  $xyt$  space, color coded by normalized local wave amplitude  $A_m$ , for the region corresponding to the lower square region of Fig. 2(d), in the  $xyt$  space. The positions of  $SR_A$  and  $SR_C$  correspond to the positions of the defects located at A and C in Fig. 3(a), respectively.

Figure 5(b) shows the plots of  $\langle N_d \rangle_s$  and  $\langle R_d \rangle_s$  versus  $N_{SR}$ .  $\langle N_d \rangle_s$  is the mean number of defects in the skeleton region of SRs (i.e., the region  $0.6c$  surrounding the projection of SR sites of the entire cluster onto the  $xy$  space), averaged over  $0.2$  s before the SR cluster starting at  $\tau = 0$  s in the  $xyt$  space.  $\langle R_d \rangle_s$  is the radius of gyrations of the above defects (i.e., the root-mean-square radial distance of those defects). Figure 5(c) shows the plots of  $\langle \Delta t_{SR} \rangle$  and  $\langle R_{SR} \rangle$  versus  $N_{SR}$ , where  $\langle \Delta t_{SR} \rangle$  and  $\langle R_{SR} \rangle$  are the averaged temporal span and the spatial span (radius of gyration of SR sites in the  $xyt$  space) of SR clusters with size  $N_{SR}$  in the  $xyt$  space.

Figure 5(a) shows that the SR cluster is preceded by the sequential rises of the amplitudes of the slow to the fast

modes, associated with deteriorating  $\langle \psi_6 \rangle_c$ . The above temporal changes are stronger for the larger cluster. The monotonic power-law increases of  $\langle N_d \rangle_s$  and  $\langle R_d \rangle_s$  with increasing  $N_{SR}$  in Fig. 5(b) indicate that the larger SR clusters are preceded by a larger number of and more spread initial defects in the skeleton region of the SR cluster. The above findings suggest that those dynamical and structural variables can be identified as precursors for extreme clusters.

Moreover, the power-law increases of  $\langle \Delta t \rangle$  and  $\langle R_{SR} \rangle$  in Fig. 5(c) clearly indicate that the larger SR cluster in the  $xyt$  space tends to have the longer temporal and larger spatial spans, respectively. In Fig. 5(a), the amplitudes of all modes reach their maxima at about the same time,  $\tau \sim 0.5\langle \Delta t \rangle$  and

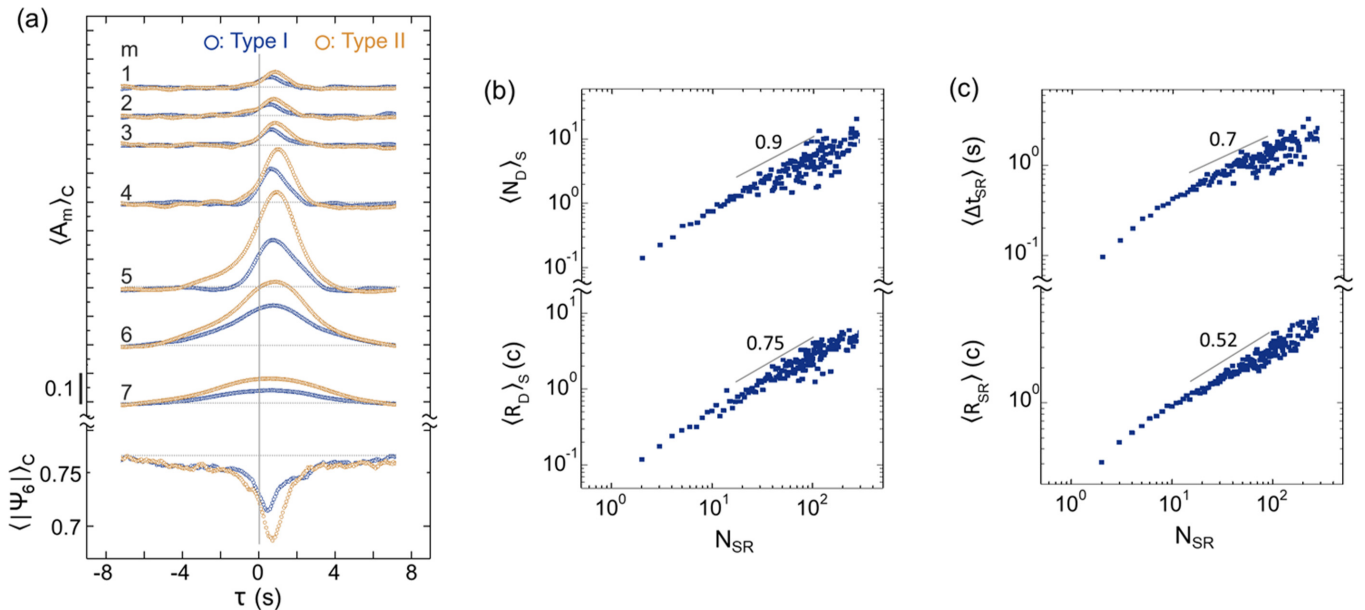


FIG. 5. (a) Waterfall plots of the temporal evolutions of  $\langle A_m \rangle_c$  of modes 1 to 7, and  $\langle \psi_6 \rangle_c$ , averaged over all the sites in the circled regions at time  $\tau$  for the type I and type II clusters. Here, the center of the circled region is the spatial center of mass of all the SR sites in the cluster, and the circle radius is  $5c$ , i.e. 1.25 times of the radius of gyration of the spatial positions of all SR sites in single type II clusters, averaged over all type II clusters. (b) Plots of  $\langle N_d \rangle_s$  and  $\langle R_d \rangle_s$  vs  $N_{SR}$ .  $\langle N_d \rangle_s$  is the mean number of defects in the skeleton region of the SR cluster (i.e., the region  $0.6c$  surrounding projection of SR sites of the entire cluster onto the  $xy$  space), averaged over  $0.2$  s before the SR cluster starting at  $\tau = 0$  s in the  $xyt$  space.  $\langle R_d \rangle_s$  is the radius of gyrations of the above defects (i.e., the root-mean-square radial distance of those defects). (c) Plots of  $\langle \Delta t_{SR} \rangle$  and  $\langle R_{SR} \rangle$  vs  $N_{SR}$ , where  $\langle \Delta t_{SR} \rangle$  and  $\langle R_{SR} \rangle$  are the averaged temporal span and spatial span (radius of gyration of SR sites in the  $xyt$  space) of SR clusters with size  $N_{SR}$  in the  $xyt$  space.

then gradually decrease. Namely, the larger temporal span with the larger SR cluster causes the rightward shifts of the peaks in Fig. 5(a). Comparing with other modes, the largest peak height of mode 5 implies its largest contribution for the avalanche activities. The sudden onsets with smaller rise of  $\langle A_m \rangle_c$  of faster modes 3 to 1 right before  $\tau = 0$  s manifest their minor roles for triggering bond breaking and avalanche SRs. The peak heights for the  $\langle A_m \rangle_c$  curves of all modes in Fig. 5(a) of the extreme clusters are larger than those of the smaller clusters.

Now we can construct a clear dynamical picture for avalanche SRs, especially for extreme avalanche SRs. Before avalanche SRs, the SR skeleton region has worse structural order. The poor particle interlocking in this region is more vulnerable to thermally induced shear oscillations along the Burgers vector direction of the defect, especially for the slow modes since they cost lower energy due to their larger spatiotemporal scales. The increasing amplitudes of slow modes with time further deteriorate structural order, and facilitate the excitations of faster modes which cause higher energies. As the amplitudes of the slow to fast modes sequentially increase, the superposition of those modes due to their phase synchronization can cause severe bond rotation and stretching, and trigger SRs through bond-breaking/reconnection. Associated with the intermittent phase synchronization of different modes of propagating transverse waves with large amplitudes, SRs can propagate with defects to other regions through cascaded bond-breaking/reconnection along the strong shear direction in a stick-slip way, once avalanche SRs start from certain defect sites.

Namely, the above process provides a feedback between evolutions of structures and multiscale dynamics for deteriorating structural order, facilitating wave excitations and defect propagations through shear induced bond-breaking/reconnection, and SR spreads. After avalanche SR ceases, defect generation and motion all stop, accompanying the gradual healing of the poor structural order, and the sequential decays of the amplitudes of fast to the slow modes.

Note that, as shown in Fig. 5(b), the larger  $\langle N_d \rangle_s$  and  $\langle R_d \rangle_s$  for the larger SR clusters indicate that, before SR avalanche, the poor structural order around initial more spread defects with larger number in the SR skeleton region facilitates the stronger excitations for multiscale shear waves. It causes cascaded bond-breakings/reconnections, leading to the larger avalanche SRs propagating along the skeleton. It is the key for inducing extreme avalanche SR activities.

## VI. EXAMPLE ILLUSTRATING THE SPATIOTEMPORAL EVOLUTIONS OF THE EXTREME AVALANCHE STRUCTURAL REARRANGEMENTS, STRUCTURAL ORDER, AND AMPLITUDES OF DIFFERENT SCALE MODES

The above dynamical picture for the extreme avalanche cluster can be further illustrated by the example showing the sequential images of particle configuration, color coded by  $|\Psi_6|$  and normalized amplitudes  $A_m$  with  $m = 2, 5$ , and  $6$ , in the left column and the right three columns of Fig. 6, respectively. In the top row of Fig. 6 ( $\tau = -3$  s), the locations of SR sites in the entire extreme avalanche SR cluster [the

same cluster as that of Fig. 2(f)], starting from  $\tau = 0$  s and ending at  $\tau = 1.5$  s, are labeled by green spheres to show their correlations with the earlier spatial distributions of  $|\Psi_6|$  and  $A_m$ , respectively. In the bottom three rows, the onset and spreading of SR sites of this extreme avalanche cluster are illustrated by the spheres color coded by the occurrence time  $\delta t$  from the time of each row. The SR sites belonging to other smaller SR clusters associated with the emergences of defects in the skeleton region of poor structural order over the above 5.5 s interval (e.g., in the three circle regions of the upper left panel of Fig. 6) are not plotted.

At first glance, the regions of low  $|\Psi_6|$  and regions with large  $A_m$  heterogeneously appear in the form of clusters and change with time. The above two types of regions are spatially and temporally correlated, with the stronger correlation for the slower modes. This is also supported by our previous findings through measuring the correlation probability between local  $|\Psi_6|$  and local  $A_m$  [42].

Even at  $\tau = -3$  s, the skeleton region with low  $|\Psi_6|$ , where  $A_5$  and  $A_6$  are also large, partially coincides with the skeleton of the extreme avalanche SR cluster starting at  $\tau = 0$  s. From  $-3$  to  $0$  s, the structural order gradually evolves associated with the increasing overlap between the above two skeleton regions. It manifests the precursor roles played by  $|\Psi_6|$ ,  $A_5$ , and  $A_6$  for the later avalanche SRs. As shown in the bottom three rows, SRs initiated at different widely spread regions from  $\tau = 0$  s rapidly spread and form a large avalanche cluster. The propagation of the SRs is led by the propagation of structure deteriorating front [also see the example in the right column of Fig. 3(a)] associated with the spreading of high  $A_m$  regions of the slow modes. Although there are many regions with poor structural order and large  $A_m$  of various modes at  $\tau = 0$  s, the phase synchronizations of various mode at limited spots (indicated by blue spheres) are the key to determine the special sites for the initiations of the extreme SR cluster.

The extreme avalanche SR cluster ends at  $\tau = 1.5$  s without new SR generations for a while. As shown in the last row of Fig. 6, the structural order around the extreme SR skeleton region for the earlier occurrence of SRs (e.g., the second quadrant region) becomes better, associated with drastically reduced  $A_m$  of the slower modes. However, the regions around the region in the later stage of the extreme avalanche SR cluster is still not fully reformed and still can support large  $A_m$ .

The above findings again manifest that SR spreading, led by the structural order deterioration associated with increasing amplitudes of slow modes, is followed by the reverse process, as also demonstrated in Figs. 3(a) and 5(a).

## VII. COMPARISON WITH SR RELATED FINDINGS IN OTHER WORKS

The recent studies of the 2D glassy state of binary mixtures and cold dusty plasma liquids demonstrate that the local or coarse-grained structural order information can be used as a short-time predictor for the subsequent local SRs [21,29,32,33]. The experimental studies using normal mode analysis in colloidal glass showed that low frequency quasilocalized phonon modes, modes representing low frequency barriers for SR, are correlated with local

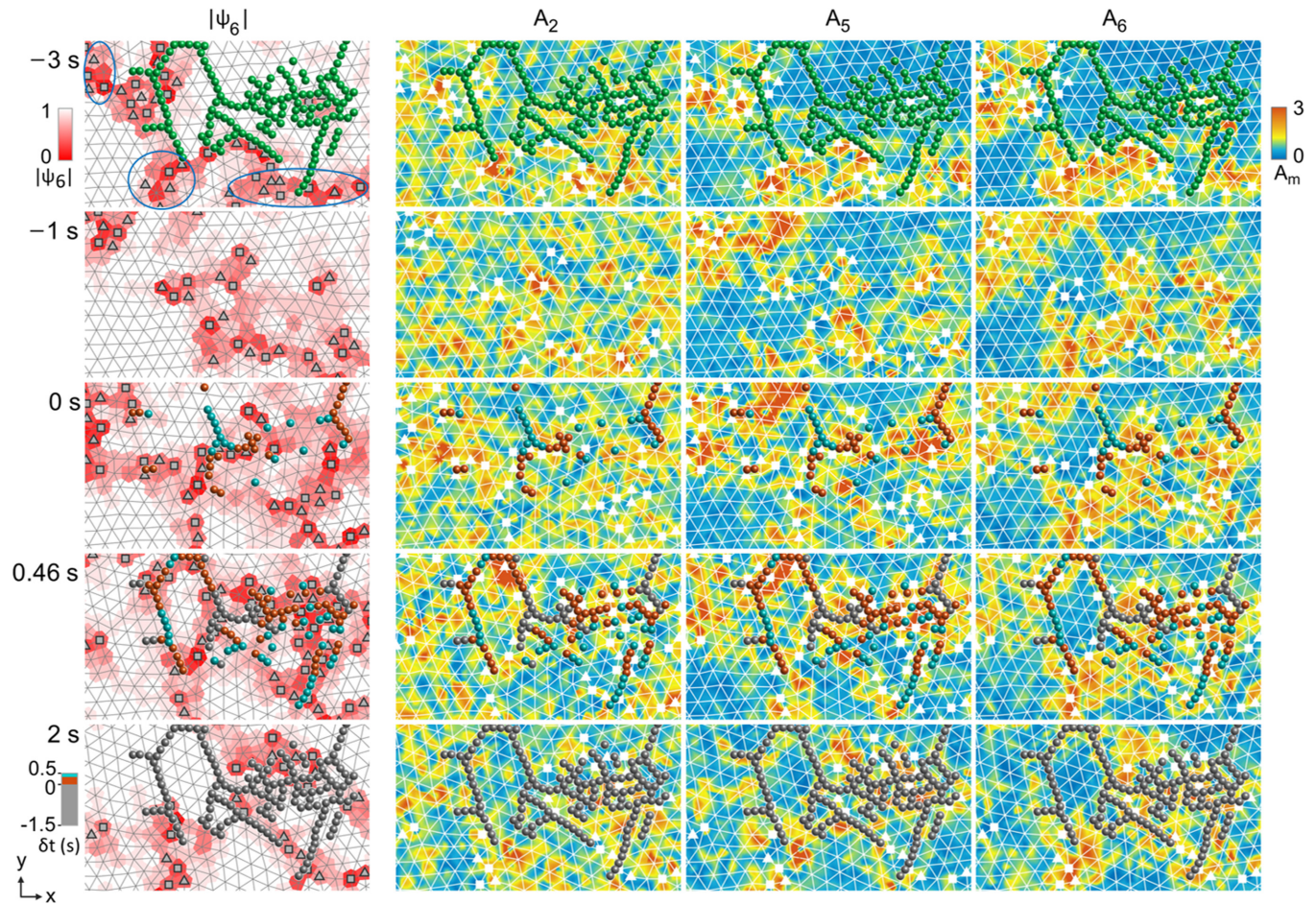


FIG. 6. Sequential images of particle configuration, color coded by  $|\Psi_6|$  (left column) and  $A_m$  (right three columns) with  $m = 2, 5,$  and  $6,$  respectively. The green spheres in the plots at  $\tau = -3$  s denote SR sites in the entire extreme avalanche SR cluster shown in Fig. 2(f). The SR sites not belonging to the extreme SR clusters are not shown (e.g., in the three circled regions). In the bottom three rows, spheres denoting SR sites of the extreme cluster are color coded by  $\delta t$ , the occurrence time of SR starting from the time of each panel.

SRs [36–39,41,42]. Other numerical studies in 2D supercooled and glass forming liquid showed that soft spots identified by the intensity of fast (high frequency) rattling provide an excellent predictor for the long-time displacement leading to cage jump and SR [26,34,35]. The spatial extent of the avalanches is strongly correlated with the extent of the spatial regions of large short-time fluctuation [26,34,35]. Nevertheless, in addition to demonstrating consistent results with the above findings, our study further provides a clear picture to unify how the interplay of the spatiotemporal evolutions of defects, local and coarse structural order, and cascaded multiscale wave excitations from the slow to the fast modes and their synchronization lead to the excitation, spreading, and termination of avalanche SRs, especially the extreme SRs in the spatiotemporal space.

Note that, for the cold liquid down to the discrete kinetic level, the interplay of stochastic thermal agitation and mutual interaction is the key determining the generic behaviors of correlations among microstructure, motion, and topological rearrangement, regardless of the differences of detailed interaction forms. Therefore, although dusty plasma liquid is a Yukawa liquid, our study demonstrates consistent results with the previous findings using various local structural and

dynamical variables as precursors for the subsequent SRs in other cold and glassy liquids. It is interesting to test whether our unified picture of how multiscale acoustic wave excitations lead to avalanche structural rearrangements can be extended to other cold or glassy liquids.

## VIII. CONCLUSION

In conclusion, using a quasi-2D cold dusty plasma liquid around freezing as a platform, we experimentally unravel how the multiscale thermal acoustic wave excitations lead to local SRs and avalanche SR activities, especially extreme avalanche SR activities, and identify their precursors, through a method based on empirical mode decomposition, which can extract the local amplitudes and phases of various modes for their spatiotemporal evolutions. The following key results are found.

(A) SRs appear in the form of avalanche clusters exhibiting scale-free cluster size distribution in the  $xyt$  space. The larger avalanche clusters are mainly composed of dendritic SRs connected to more aggregated SRs, with larger spatial and temporal spans. (B) The Burgers vector direction of the dislocation defect determines the direction of the strong shear strip between the two adjacent corotating CODs. The



intermittent phase synchronization of propagating shear wave modes with large amplitudes is the key for triggering and sustaining the stick-slip propagation of SRs along the strong shear strip, and forming dendritic SRs. (C) The regions of poor structural order and regions with large wave amplitudes heterogeneously appear in the form of clusters and changes with time. The larger spatial scales of the slower modes cause less strain energies. It facilitates the easier excitations of slower modes in the region of poor structural order, which deteriorates local structural order and in turn facilitates local faster mode excitations. (D) The sequential rises of the amplitudes of waves from the slow to the fast modes with deteriorating structural order through the dynamical feedback in (C), and the intermittent spatiotemporal synchronization of all modes, are the keys for the onset and propagation of SRs in large SR clusters, along the preceding large skeleton of poor structural order. (E) After the gradual release of the local strain energy through SR spreading, the wave amplitudes sequentially decrease from the faster modes to the slower modes. (F) The earlier and stronger rises of coarse-grained amplitudes from the slow to the fast modes and the larger preceded skeleton of poor structural order around more and widely spread defects can be used as precursors for warning extreme avalanche SRs.

Dusty plasma liquid is a good platform to mimic and understand many generic features of liquids at the discrete kinetic level. This study provides a clear picture to unify how the interplay of the spatiotemporal evolutions of defects, local and coarse-grained structural order, and cascaded multiscale wave excitations and their phase synchronization lead to the excitation, spreading, and termination of avalanche SRs, especially extreme SRs in the spatiotemporal space. It aids understanding and opens a new window to study the avalanche SRs and

identify their precursors in various cold and glass-forming liquids or glasses.

#### ACKNOWLEDGMENT

This work is supported by the Ministry of Science and Technology, Taiwan, under Contract No. 110-2112-M-008-007.

#### APPENDIX A: BOND ORIENTATIONAL ORDER AND ISOPHASE SURFACE PLOTTING

The Bond-orientational order  $\Psi_6$  is defined as  $\Psi_6(r_i) = \frac{1}{N_i} \sum_j \exp(i6\theta_{i,j})$ , where  $\theta_{i,j}$  is the angle of the vector from the particle at  $r_i$  to its  $j$ th nearest neighbor, and  $N_i$  is the number of the nearest neighbors [61].  $|\Psi_6| = 1$  at the perfect sixfold lattice sites and  $< 0.4$  for the defect sites, respectively.

To plot the isophase surface,  $A_{\alpha,m}(t)$  and  $\phi_{\alpha,m}(t)$  from  $D_{\alpha,m}(t)$  for each adjacent particle pair  $\alpha$  in the  $xy$  plane at time  $t$  are first measured, and assigned as the  $A_m(t)$  and  $\phi_m(t)$  at the center position of each pair, respectively. Through triangulation-based cubic interpolation,  $A_m(\mathbf{x}, t)$  and  $\phi_m(\mathbf{x}, t)$  over the entire  $xy$  space can be obtained, and the isophase surfaces color coded by  $A_m$  in the  $xyt$  space can be plotted.

#### APPENDIX B: STRUCTURAL REARRANGEMENTS AND DEFECT MOTIONS ALONG SHEAR STRIPS WITH 120° ANGLE DIFFERENCE

The three panels of Fig. 7(a) are plotted in the same ways as those of Figs. 2(a) to 2(c). It shows another example at different time  $t = 4$  s, illustrating the correlations of particle

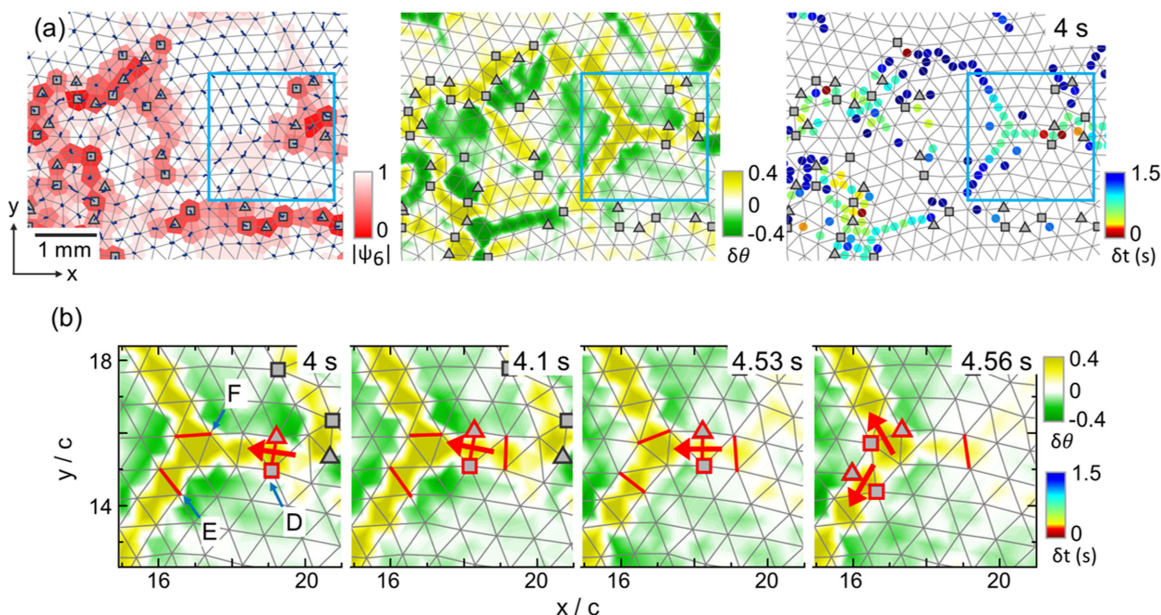


FIG. 7. (a) Another example at time  $t = 4$  s, using the same plotting ways as those of Figs. 2(a) to 2(c), to illustrate the correlations of particle configuration, heterogeneous structural order, COD rotation, and avalanche SRs with various sizes. (b) Sequential snapshots from the squared region of (a) showing an example of how the corotations of three adjacent CODs lead to the formation of the Y-shaped strong shear skeleton, along which SRs propagate with defects.

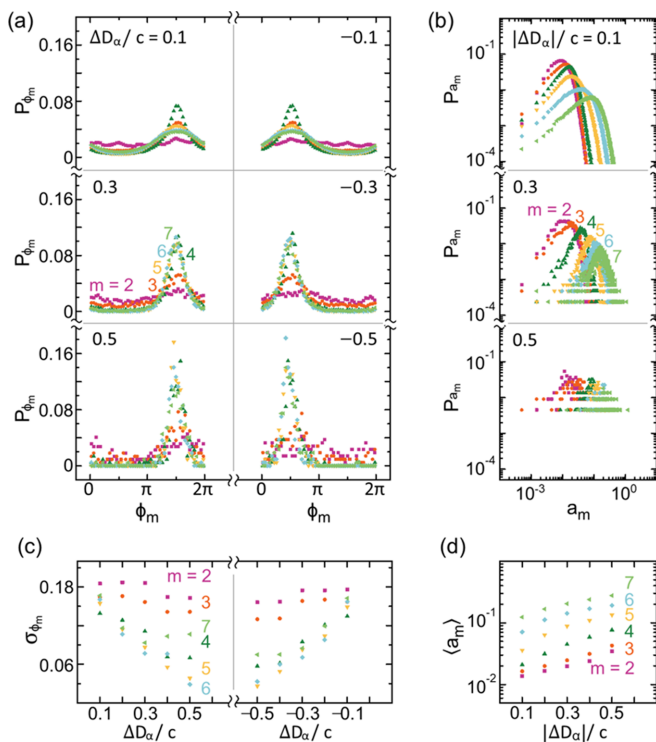


FIG. 8. (a) Histograms of the phases  $\phi_m$  of modes 2 to 7 and times for events with  $\Delta D_\alpha = 0.1c, 0.3c,$  and  $0.5c$  (left column) and  $\Delta D_\alpha = -0.1c, -0.3c,$  and  $-0.5c$  (right column). (b) Histograms of  $a_m$  of modes 2 to 7 at times for events with  $|\Delta D_\alpha| = 0.1c, 0.3c,$  and  $0.5c$ . (c) Plots of  $\sigma_{\phi_m}$  (the standard deviation of  $\phi_m$  in the  $\phi_m$  histogram) vs  $\Delta D_\alpha$ . (d) Plots of  $\langle a_m \rangle$  (average of  $a_m$ ) vs  $\Delta D_\alpha$ .

configuration, heterogeneous structural order, COD rotation, and avalanche SRs with various sizes. The sequential snapshots of Fig. 7(b) from the squared region of Fig. 7(a) give an example of how the corotations of three adjacent CODs lead to the formation of Y-shaped skeleton, along which SR propagates with the defect for forming dendritic SR branches. The red arrows denote defect (SR) propagating direction, normal to the bond connecting the five- and the sevenfold disclination defects. The excitation of the three corotation CODs causes the formation of three connected strong shear strips with  $120^\circ$  separation, along which the defect from site D

at 4 s propagates leftward. It then dissociates into two defects, which further propagate along the left two shear strips, in a stick-slip way and reach sites E and F at 5.1 s.

This dissociation from one to two dislocations is under the conservation of Burgers vectors [28,61]. On the other hand, the reverse process with two defects propagating along two shear strips  $120^\circ$  apart and combining into one defect can also occur, and the corresponding Burgers vector is conserved [28,61]. It is also one of the causes for the formation of the dendritic SR structure. Similar to the findings of the 2D cold liquid sheared by the weak external stress [28], if the special directions of the final Burgers vector of the remaining defects cannot allow their further reduction mainly through recombination, the region can be ruptured and healed through the excitation of very small CODs which lead to the formation dense SR aggregations after defects propagate along dendritic strips.

### APPENDIX C: PHASE SYNCHRONIZATION OF MULTISCALE WAVE MODES

As shown in Fig. 3(d), there are strong correlations between  $D_\alpha$ , and the phases and the amplitudes of various wave modes. The large rise of  $D_\alpha$  which causes SR and defect motion is associated with the synchronization of the strong ascending (or rising) parts of the  $D_{\alpha,m}$  of various modes. To statistically support this observation, the left and right columns of Fig. 8(a) show the probability distribution functions of  $\phi_m$  and  $a_m$  (the amplitude of mode  $m$ ) of modes 2 to 7 at times for events with  $\Delta D_\alpha = 0.1c, 0.3c,$  and  $0.5c$ , and  $\Delta D_\alpha = -0.1c, -0.3c,$  and  $-0.5c$ , respectively.  $\Delta D_\alpha$  is defined as  $\Delta D_\alpha = D_\alpha(t + \Delta t/2)D_\alpha(t - \Delta t/2)$ , the change of  $D_\alpha$  over time interval  $\Delta t = 0.3$  s. Figure 8(b) shows the probability distribution functions of  $a_m$  for  $|\Delta D_\alpha| = 0.1c, 0.3c,$  and  $0.5c$ . Figures 8(c) and 8(d) further show the plots of  $\sigma_{\phi_m}$  (the standard deviation of  $\phi_m$ ) and  $\langle a_m \rangle$  (the averaged of  $a_m$ ) versus  $|\Delta D_\alpha|$ , respectively.

Figure 8(a) indicates that with increasing  $\Delta D_\alpha$  and  $-\Delta D_\alpha$ , and increasing  $m$  for  $m > 2$ ,  $\phi_m$  of different modes tend to peak around  $3\pi/2$  and  $\pi/2$  (i.e., corresponding to the strongest increasing and decreasing parts of  $D_{\alpha,m}$ ), respectively, and the  $\phi_m$  histogram becomes narrower, as also evidenced by the plots of standard deviation  $\sigma_{\phi_m}$  versus  $\Delta D_\alpha$  in Fig. 8(c). Figure 8(b) indicates that the peaks of the probability

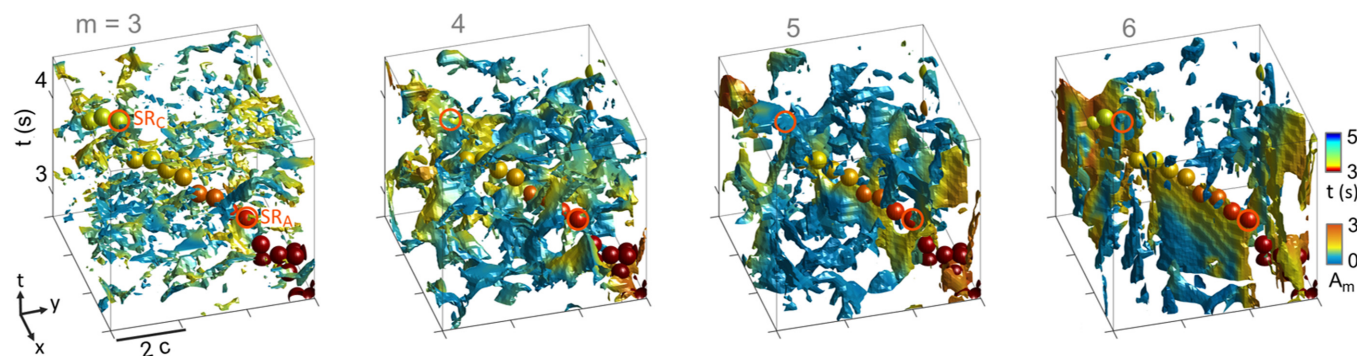


FIG. 9. The complete plots of isophase ( $\phi_m = 3\pi/2$ ) surfaces of modes 3 to 6, color coded by  $A_m$  in the  $xyt$  space. The spheres are SR sites color coded by their occurrence time  $t$ .

distribution functions of  $a_m$  shift rightward with increasing  $|\Delta D_\alpha|$  and increasing  $m$ , as also evidenced by the increasing  $\langle a_m \rangle$  with increasing  $|\Delta D_\alpha|$  and  $m$  in Fig. 8(d). Namely, to form a larger  $|\Delta D_\alpha|$ , the large amplitudes of all modes and the stronger synchronization of modes with  $m > 2$ , especially of the slower modes 4 to 6, are needed. The absence of phase synchronization for mode 2 is due to our  $\Delta t$  being longer

than the typical period of this mode. Note that the statistics of mode 1 is not shown because our image frame rate is not high enough to accurately resolve its phase. Figure 9 shows the complete plots of isophase ( $\phi_m = 3\pi/2$ ) surfaces of modes 3 to 6, color coded by  $A_m$  in the  $xyt$  space, corresponding to the plots in Fig. 4. The spheres are SR sites color coded by their occurrence time  $t$ .

- 
- [1] J. P. Sethna, K. A. Dahmen, and C. R. Meyers, Crackling noise, *Nature (London)* **410**, 242 (2001).
  - [2] Z. Danku and F. Kun, Temporal and Spacial Evolution of Bursts in Creep Rupture, *Phys. Rev. Lett.* **111**, 084302 (2013).
  - [3] A. Shekhawat, S. Zapperi, and J. P. Sethna, From Damage Percolation to Crack Nucleation Through Finite Size Criticality, *Phys. Rev. Lett.* **110**, 185505 (2013).
  - [4] A. Ghosh, Z. Budrikis, V. Chikkadi, A. L. Sellerio, S. Zapperi, and P. Schall, Direct Observation of Percolation in the Yielding Transition of Colloidal Glasses, *Phys. Rev. Lett.* **118**, 148001 (2017).
  - [5] A. Helmstetter, Is Earthquake Triggering Driven by Small Earthquakes?, *Phys. Rev. Lett.* **91**, 058501 (2003).
  - [6] G. Niccolini, A. Carpinteri, G. Lacidogna, and A. Manuello, Acoustic Emission Monitoring of the Syracuse Athena Temple: Scale Invariance in the Timing of Ruptures, *Phys. Rev. Lett.* **106**, 108503 (2011).
  - [7] J. Davidsen and A. Green, Are Earthquake Magnitudes Clustered?, *Phys. Rev. Lett.* **106**, 108502 (2011).
  - [8] W. Cai and L. Chen, F. Ghanbarnejad, and P. Grassbergerr, Avalanche outbreaks emerging in cooperative contagions, *Nat. Phys.* **11**, 936 (2015).
  - [9] S. V. Buldyrev, R. Parshani, G. Paul, H. E. Stanley, and S. Havlin, Catastrophic cascade of failures in interdependent networks, *Nature (London)* **464**, 1025 (2010).
  - [10] J. Gao, S. V. Buldyrev, H. Stanley, and S. Havlin, Networks formed from interdependent networks, *Nat. Phys.* **8**, 40 (2012).
  - [11] J. Wang, S. Kádár, P. Jung, and K. Showalter, Noise Driven Avalanche Behavior in Subexcitable Media, *Phys. Rev. Lett.* **82**, 855 (1999).
  - [12] P. Bak, C. Tang, and K. Wiesenfeld, Self-Organized Criticality: An Explanation of the  $1/f$  Noise, *Phys. Rev. Lett.* **59**, 381 (1987).
  - [13] H. Jensen, *Self-Organized Criticality* (Cambridge University Press, Cambridge, 1998).
  - [14] O. Ramos, E. Altshuler, and K. J. Måløy, Avalanche Prediction in a Self-Organized Pile of Beads, *Phys. Rev. Lett.* **102**, 078701 (2009).
  - [15] F. H. Stillinger, Relaxation and flow mechanisms in fragile glassforming liquids, *J. Chem. Phys.* **89**, 6461 (1988).
  - [16] M. M. Hurley and P. Harrowell, Kinetic structure of a two-dimensional liquid, *Phys. Rev. E* **52**, 1694 (1995).
  - [17] Y. J. Lai and L. I., Avalanche Excitations of Fast Particles in Quasi-2D Cold Dusty-Plasma Liquids, *Phys. Rev. Lett.* **89**, 155002 (2002).
  - [18] T. Kawasaki, T. Araki, and H. Tanaka, Correlation between Dynamic Heterogeneity and Medium-Range Order in Two-Dimensional Glass-Forming Liquids, *Phys. Rev. Lett.* **99**, 215701 (2007).
  - [19] Y. Han, N. Y. Ha, A. M. Alsayed, and A. G. Yodh, Melting of two-dimensional tunable-diameter colloidal crystals, *Phys. Rev. E* **77**, 041406 (2008).
  - [20] L. Assoud, F. Ebert, P. Keim, R. Messina, G. Maret, and H. Löwen, Ultrafast Quenching of Binary Colloidal Suspensions in an External Magnetic Field, *Phys. Rev. Lett.* **102**, 238301 (2009).
  - [21] Y. S. Su, Y. H. Liu, and L. I., Correlating Structural Order with Structural Rearrangement in Dusty Plasma Liquids: Can Structural Rearrangement be Predicted by Static Structural Information?, *Phys. Rev. Lett.* **109**, 195002 (2012).
  - [22] Y. S. Su, V. W. Io, and L. I., Transient slowing down relaxation dynamics of the supercooled dusty plasma liquid after quenching, *Phys. Rev. E* **86**, 016405 (2012).
  - [23] I. V. Schweigert, V. A. Schweigert, A. Melzer, and A. Piel, Melting of dust plasma crystals with defects, *Phys. Rev. E* **62**, 1238 (2000).
  - [24] E. R. Weeks, J. C. Crocker, A. C. Levitt, A. Schofield, and D. A. Weitz, Three-dimensional direct imaging of structural relaxation near the colloidal glass transition, *Science* **287**, 627 (2000).
  - [25] C. Reichhardt and C. J. O. Reichhardt, Fluctuating Topological Defects in 2D Liquids: Heterogeneous Motion and Noise, *Phys. Rev. Lett.* **90**, 095504 (2003).
  - [26] R. Candelier, A. Widmer-Cooper, J. K. Kummerfeld, O. Dauchot, G. Biroli, P. Harrowell, and D. R. Reichman, Spatiotemporal Hierarchy of Relaxation Events, Dynamical Heterogeneities, and Structural Reorganization in a Supercooled Liquid, *Phys. Rev. Lett.* **105**, 135702 (2010).
  - [27] C. Yang, C. W. Io, and L. I., Cooperative-Motion-Induced Structural Evolution in Dusty-Plasma Liquids with Microheterogeneity: Rupture, Rotation, Healing, and Growth of Ordered Domains, *Phys. Rev. Lett.* **109**, 225003 (2012).
  - [28] C. Yang, W. Wang, and L. I., Avalanche structural rearrangement through cracking-healing in weakly stressed cold dusty plasma liquids, *Phys. Rev. E* **93**, 013202 (2016).
  - [29] H. Tanaka, H. Tong, R. Shi, and J. Russo, Revealing key structural features hidden in liquids and glasses, *Nat. Rev. Phys.* **1**, 333 (2019).
  - [30] E. D. Cubuk, S. S. Schoenholz, J. M. Rieser, B. D. Malone, J. Rottler, D. J. Durian, E. Kaxiras, and A. J. Liu, Identifying Structural Flow Defects in Disordered Solids Using Machine-Learning Methods, *Phys. Rev. Lett.* **114**, 108001 (2015).
  - [31] S. S. Schoenholz, E. D. Cubuk, D. M. Sussman, E. Kaxiras, and A. J. Liu, A structural approach to relaxation in glassy liquids, *Nat. Phys.* **12**, 469 (2016).

- [32] H. Tong and H. Tanaka, Revealing Hidden Structural Order Controlling Both Fast and Slow Glassy Dynamics in Supercooled Liquids, *Phys. Rev. X* **8**, 011041 (2018).
- [33] H. Tong and H. Tanaka, Structural order as a genuine control parameter of dynamics in simple glass formers, *Nat. Commun.* **10**, 5596 (2019).
- [34] A. Widmer-Cooper and P. Harrowell, Predicting the Long-Time Dynamic Heterogeneity in a Supercooled Liquid on the Basis of Short-Time Heterogeneities, *Phys. Rev. Lett.* **96**, 185701 (2006).
- [35] L. Berthier and R. L. Jack, Structure and dynamics of glass formers: Predictability at large length scales, *Phys. Rev. E* **76**, 041509 (2007).
- [36] A. Widmer-Cooper, H. Perry, P. Harrowell, and D. R. Reichman, Irreversible reorganization in a supercooled liquid originates from localized soft modes, *Nat. Phys.* **4**, 711 (2008).
- [37] K. Chen, M. L. Manning, P. J. Yunker, W. G. Ellenbroek, Z. Zhang, A. J. Liu, and A. G. Yodh, Measurement of Correlations between Low-Frequency Vibrational Modes and Particle Rearrangements in Quasi-Two-Dimensional Colloidal Glasses, *Phys. Rev. Lett.* **107**, 108301 (2011).
- [38] A. Ghosh, V. Chikkadi, P. Schall, and D. Bonn, Connecting Structural Relaxation with the Low Frequency Modes in a Hard-Sphere Colloidal Glass, *Phys. Rev. Lett.* **107**, 188303 (2011).
- [39] S. S. Schoenholz, A. J. Liu, R. A. Riggleman, and J. Rottler, Understanding Plastic Deformation in Thermal Glasses from Single-Soft-Spot Dynamics, *Phys. Rev. X* **4**, 031014 (2014).
- [40] H. Shintani and H. Tanaka, Universal link between the boson peak and transverse phonons in glass, *Nat. Mater.* **7**, 870 (2008).
- [41] H. Tong and N. Xu, Order parameter for structural heterogeneity in disordered solids, *Phys. Rev. E* **90**, 010401(R) (2014).
- [42] H. W. Hu, W. W. and L. I, Multiscale Coherent Excitations in Microscopic Acoustic Wave Turbulence of Cold Dusty Plasma Liquids, *Phys. Rev. Lett.* **123**, 065002 (2019).
- [43] N. E. Huang, Z. Shen, S. R. Long, M. C. Wu, H. H. Shih, Q. Zheng, N. C. Yen, C. C. Tung, and H. H. Liu, The empirical mode decomposition and the Hilbert spectrum for nonlinear and non-stationary time series analysis, *Proc. R. Soc. London A* **454**, 903 (1998).
- [44] N. E. Huang, M. C. Wu, S. R. Long, S. S. P. Shen, W. Qu, P. Gloersen, and K. L. Fan, A confidence limit for the empirical mode decomposition and Hilbert spectral analysis, *Proc. R. Soc. London A* **459**, 2317 (2003).
- [45] N. E. Huang and Z. A. Wu, A review on Hilbert-Huang transform: Method and its applications to geophysical studies, *Rev. Geophys.* **46**, RG2006 (2008).
- [46] J. R. Yeh, J. S. Shieh, and N. E. Huang, Complementary ensemble empirical mode decomposition: A novel noise enhanced data analysis method, *Adv. Adapt. Data Anal.* **02**, 135 (2010).
- [47] V. Nosenko, J. Goree, and A. Piel, Cutoff Wave Number for Shear Waves in a Two-Dimensional Yukawa System (Dusty Plasma), *Phys. Rev. Lett.* **97**, 115001 (2006).
- [48] A. Piel, D. Block, A. Melzer, M. Mulsow, J. Schablinski, A. Schella, F. Wieben, and J. Wilms, Microphysics of liquid complex plasmas in equilibrium and non-equilibrium systems, *Eur. Phys. J. D* **72**, 80 (2018).
- [49] P. C. Lin and L. I, Interacting Multiscale Acoustic Vortices as Coherent Excitations in Dust Acoustic Wave Turbulence, *Phys. Rev. Lett.* **120**, 135004 (2018).
- [50] P. C. Lin and L. I, Synchronization of multiscale waveform focusing for rogue wave generation in dust acoustic wave turbulence, *Phys. Rev. Research* **2**, 023090 (2020).
- [51] J. L. Jou, W. S. Lo, and L. I, Rogue wave generation in wind-driven water wave turbulence through multiscale phase-amplitude coupling, phase synchronization, and self-focusing by curved crests, *Phys. Fluids* **32**, 122120 (2020).
- [52] S. Nunomura, S. Zhdanov, D. Samsonov, and G. Morfill, Wave Spectra in Solid and Liquid Complex (Dusty) Plasmas, *Phys. Rev. Lett.* **94**, 045001 (2005).
- [53] L. Couëdel, V. Nosenko, M. Rubin-Zuzic, S. Zhdanov, Y. Elskens, T. Hall, and A. V. Ivlev, Full melting of a two-dimensional complex plasma crystal triggered by localized pulsed laser heating, *Phys. Rev. E* **97**, 043206 (2018).
- [54] C. A. Knapik, D. Samsonov, S. Zhdanov, U. Konopka, and G. E. Morfill, Recrystallization of a 2D Plasma Crystal, *Phys. Rev. Lett.* **98**, 015004 (2007).
- [55] Y. Feng, J. Goree, and B. Liu, Solid Superheating Observed in Two-Dimensional Strongly Coupled Dusty Plasma, *Phys. Rev. Lett.* **100**, 205007 (2008).
- [56] G. E. Morfill and A. V. Ivlev, Complex plasmas: An interdisciplinary research field, *Rev. Mod. Phys.* **81**, 1353 (2009).
- [57] N. P. Kryuchkov, E. V. Yakovlev, E. A. Gorbunov, L. Couëdel, A. M. Lipaev, and S. O. Yurchenko, Thermoacoustic Instability in Two-Dimensional Fluid Complex Plasmas, *Phys. Rev. Lett.* **121**, 075003 (2018).
- [58] J. Ashwin and A. Sen, Microscopic Origin of Shear Relaxation in a Model Viscoelastic Liquid, *Phys. Rev. Lett.* **114**, 055002 (2015).
- [59] M. Nambu, S. V. Vladimirov, and P. K. Shukla, Attractive forces between charged particulates in plasmas, *Phys. Lett. A* **203**, 40 (1995).
- [60] K. J. Strandburg, *Bond-Orientational Order in Condensed Matter Systems* (Springer, New York, 1992).
- [61] See Supplemental Material at <http://link.aps.org/supplemental/10.1103/PhysRevResearch.4.023116> for Videos S1 and S2. Video S1 shows SR sites in the  $xyt$  space from Fig. 2(d), viewing at different angles. The SR sites denoted by the spheres in each cluster is color coded by the cluster size normalized by the mean. Video S2 shows the complete plots of Fig. 4 with isophase ( $\phi_m = 1.5\pi$ ) surfaces, color coded by normalized amplitude  $A_m$ , for modes 3 to 6 in the  $xyt$  space viewing at different times and angles.
- [62] D. R. Nelson, *Defects and Geometry in Condensed Matter Physics* (Cambridge University Press, Cambridge, UK, 2002).